Materials and Design 107 (2016) 478–490

Contents lists available at ScienceDirect

Materials and Design

journal homepage: www.elsevier.com/locate/matdes

Determination of residual stress distributions in polycrystalline alumina using fluorescence microscopy

Chris A. Michaels, Robert F. Cook *

Materials Measurement Science Division, National Institute of Standards and Technology, Gaithersburg, MD 20899, USA

ARTICLE INFO

Article history:
Received 27 April 2016
Received in revised form 14 June 2016
Accepted 15 June 2016
Available online 16 June 2016

Keywords:
Residual stress
Alumina
Fluorescence
Ruby
Mapping
Microcracking

ABSTRACT

Maps of residual stress distributions arising from anisotropic thermal expansion effects in a polycrystalline alumina are generated using fluorescence microscopy. The shifts of both the R1 and R2 ruby fluorescence lines of Cr in alumina are used to create maps with sub-μm resolution of either the local mean and shear stresses or local crystallographic *a*- and *c*-stresses in the material, with approximately ±1 MPa stress resolution. The use of single crystal control materials and explicit correction for temperature and composition effects on line shifts enabled determination of the absolute values and distributions of values of stresses. Temperature correction is shown to be critical in absolute stress determination. Experimental determinations of average stress parameters in the mapped structure are consistent with assumed equilibrium conditions and with integrated large-area measurements. Average crystallographic stresses of order hundreds of MPa are determined with characteristic distribution widths of tens of MPa. The stress distributions reflect contributions from individual clusters of stress in the structure; the cluster size is somewhat larger than the grain size. An example application of the use of stress maps is shown in the calculation of stress-intensity factors for fracture in the residual stress field.

Published by Elsevier Ltd.

1. Introduction

Single crystal alumina (Al_2O_3, corundum) has a trigonal crystal structure that exhibits anisotropic thermal expansion: The coefficient of thermal expansion (CTE) is greater along the crystallographic *c*-axis than in the basal plane that contains the three *a*-axes perpendicular to the *c*-axis. [1]. As a consequence, on cooling an unconstrained corundum single crystal the *c*-axis contracts more than the *a*-axes (contraction is isotropic in the basal plane), leading to an anisotropic stress-free strain state. On cooling *polycrystalline* Al_2O_3 from a high temperature, however, the mutual constraint of neighboring unaligned grains impedes the free CTE strains for an individual grain and residual stress fields are developed in the polycrystalline microstructure in reaction to the constraint [2]. Considerations of mechanical equilibrium for a polycrystal in which the grains are randomly oriented show that the mean normal stress in the crystallographic *c*-direction is tensile, $\overline{\sigma}_c>0$, and that in the *a*-direction is compressive, $\overline{\sigma}_a<0$ [3]. Mechanical equilibrium requires the mean spherical stress in the microstructure be zero, $\overline{\sigma}_M = 0$, such that the mean normal stresses in the crystallographic frame have the relationship $\overline{\sigma}_c = -2\overline{\sigma}_a$. Estimates for the magnitudes of these stresses on cooling polycrystalline Al_2O_3 from typical sintering temperatures are approximately 100 MPa, although the value depends on grain size, grain shape, the presence of other phases, and cooling rate [2,4–7].

The nature of the microstructurally-driven residual stress field significantly affects the mechanical properties, especially fracture, of polycrystalline Al_2O_3. At the smallest length scale, residual tensile stresses can be relieved in the structure on cooling through the formation of spontaneous "microcracks"; these are typically localized to fracture of a single grain boundary facet or grain, and occur most frequently in large-grained materials [7–10]. Such microcracks form preferential locations for material removal under erosion or wear conditions and form strength-limiting flaws in structural applications. At an intermediate scale, sharp surface contacts generate localized plastic deformation zones in the material with attendant tensile stress fields that initiate and stabilize cracks, typically a few grain diameters in length [11]. The microstructural residual stress field can significantly impede or assist in the formation of such contact flaws, leading to significant strength degradation and potential material removal [9,12]. At the largest length scale, long cracks traversing many grains in polycrystalline ceramics are often observed to have microstructural elements behind the crack tip acting to restrain crack opening and thus impede crack propagation [13,14]. Such elements are particularly pervasive in Al_2O_3 and typically consist of either ligamentary bridges of a few grains formed by discontinuous crack propagation or frictional interlocks at a single grain boundary facet perpendicular to the predominant crack propagation direction [15]. In both cases, the local microstructural residual stress field is critical to the formation and subsequent deformation of the

* Corresponding author.
E-mail addresses: chris.michaels@nist.gov (C.A. Michaels), robert.cook@nist.gov (R.F. Cook).

http://dx.doi.org/10.1016/j.matdes.2016.06.063
0264-1275/Published by Elsevier Ltd.

restraining elements [15,16]. Such elements lead to significant increases in the toughness of the material with increases in crack length [9,12,15].

As a consequence of the above effects, knowledge of the microstructurally-driven residual stress field is critical in materials selection and design considerations for polycrystalline Al_2O_3. If the magnitude of the residual stress field is too large, the material will be prone to microcracking and hence would not be a good choice for applications in which resistance to small cracks is important, *e.g.*, a wear-resistant coating. If the magnitude of the residual stress field is too small, the material will not exhibit much microstructural toughening and hence would not be a good choice for applications in which resistance to large cracks is important, *e.g.*, a hermetic feed-through. If the distribution of the residual stress field is too heterogeneous, the material will exhibit variable crack initiation response at sharp contacts and hence would not be a good choice for applications in which strength predictability is important, *e.g.*, a radar window. Hence, in order to optimize fabrication methods for polycrystalline Al_2O_3 so as to generate microstructures appropriate for specific applications, and to predict how a given microstructure will perform, a method is required that can measure and map polycrystalline Al_2O_3 residual stress distributions.

A method with sufficient spatial and stress resolution for mapping microstructure-related stress distributions in Al_2O_3 is fluorescence microscopy. The method is based on the shift in the fluorescence bands associated with Cr, a ubiquitous substitutional impurity for Al in Al_2O_3 [17]. The crystal field arising from the octahedral arrangement of O ions surrounding the Cr ions in Al_2O_3 leads to two closely-separated R1 and R2 bands that fluoresce at a wavelength of approximately 694 nm. It is this fluorescence that gives ruby (Al_2O_3:Cr) its characteristic red color. Applications of stress, changes in temperature, and different Cr compositions all distort the octahedra and associated crystal field and lead to shifts in the energies of the R1 and R2 fluorescence peaks. Early application of this phenomenon was the incorporation of calibrated ruby chips into diamond anvil cells for use as pressure gauges during high-pressure experiments [18]. Subsequent application was the measurement and mapping of stress in single-crystal and polycrystalline Al_2O_3, although works considering two-dimensional (2-D) mapping of microstructural residual stresses are few. A recent work [19] significantly extended spatial and stress resolution for 2-D Al_2O_3 stress mapping, in addition to introducing new stress-mapping methodologies. In that work, stress in a series of Cr-doped polycrystalline Al_2O_3 materials was mapped with sub-micrometer spatial resolution and about 10 MPa stress resolution. The work used the intensities and shifts of the R1 peak to define grain boundaries in the microstructures and generate σ_c stress maps, respectively. Scales for the stress maps were determined from the R1 peak-shift distributions and assumed Gaussian stress distributions. The work [19] provides a brief but comprehensive review of application of Cr fluorescence shift to stress measurement, with an emphasis on 2-D mapping.

Here, stress mapping in polycrystalline Al_2O_3 is further extended with attention focused on stress distribution determination. The determination includes four new and important experimental and analytical features: First, the determination is accomplished by using information from *both the R1 and R2* peak shifts, significantly increasing the precision of the stress determination. Second, stress determination includes explicit *correction for temperature* changes during mapping, significantly increasing the accuracy of the stress determination—in fact, it will be shown that temperature correction is critical to obtaining absolute estimates of stress. Third, *no particular form for the stress distributions* will be assumed. Fourth, the maps will *divide the stress in two ways*, providing both local spherical and shear, as well as *a*- and *c*-direction, stress distributions. As before [19], stress determination will involve a correction for the effect of Cr composition on peak shift. In addition to generating information regarding residual stress distributions, the measurements will enable an experimental test of the equalities given above for the equilibrium mean stress values: $\overline{\sigma}_M = 0$ and $\overline{\sigma}_c = -2\overline{\sigma}_a$. The next section develops the piezospectroscopic analysis required to convert R1 and R2 fluorescence peak shifts into stress maps and distributions, including comparisons with previously used large-area scans. Also included is a brief description of the fracture mechanics analysis employed in an example application of stress mapping in predicting the behavior of microcracks. This is followed by a description of the experimental methods, which are similar to those of the previous work. The results are presented first as maps and histograms of fluorescence intensity and shifts, and then as 2-D stress maps and histograms of stress distributions. Discussion centers on comparison of the results obtained here with those obtained in prior fluorescence-based residual stress studies of Al_2O_3, the likely next steps in advancing the quantification of residual stress mapping using fluorescence, and comparison of the fluorescence mapping technique with techniques used to assess residual stress in other material systems.

2. Analysis

2.1. Stress optical analysis for mapping

The energies, ν, (in wavenumbers, cm^{-1}) of the R1 and R2 fluorescence lines in Al_2O_3:Cr are given by [20–23]

$$\nu^{(1)} = \nu_0^{(1)} + \Delta\nu^{(1)} + \Delta\nu_T^{(1)} + \Delta\nu_C^{(1)} \tag{1a}$$

$$\nu^{(2)} = \nu_0^{(2)} + \Delta\nu^{(2)} + \Delta\nu_T^{(2)} + \Delta\nu_C^{(2)}, \tag{1b}$$

where the superscripts $^{(1)}$ and $^{(2)}$ here and throughout indicate parameters associated with the R1 and R2 lines, respectively. The ν_0 values are the energies or line positions of a reference material in the unstressed state at a reference temperature (here taken to be 298.8 K) with negligible Cr composition (here taken to be undoped sapphire). Fig. 1 shows example spectra taken from single (pixel) locations on a sapphire reference and a polycrystalline Al_2O_3:Cr material. The ν_0 values of the R1 and R2 lines of the sapphire are indicated, as are the total shifts, $\Delta\nu + \Delta\nu_T + \Delta\nu_C$, for the polycrystalline material. The shifts in line positions associated with changes in temperature and composition, $\Delta\nu_T$ and $\Delta\nu_C$ respectively, will be considered below. Here attention is first focused on the shift associated with stress, $\Delta\nu$. In hyperspectral fluorescence mapping, a spectrum of fluorescence intensity as a function of wavenumber, $I(\nu)$, similar to that in Fig. 1, is obtained at every point in a map. The spectra are then analyzed to obtain $\Delta\nu$ at every point in the map, such that stress maps can be generated.

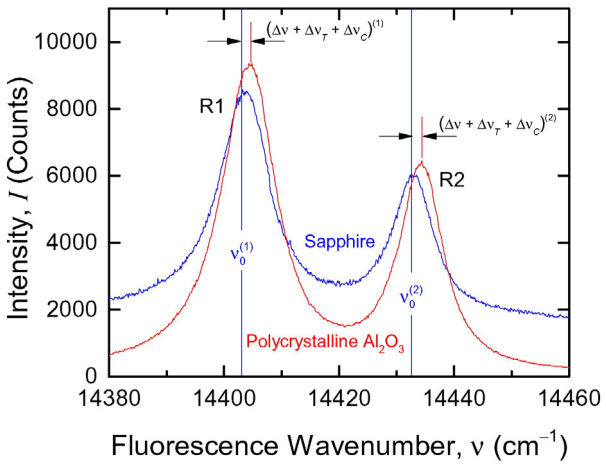

Fig. 1. Single location fluorescence spectra of single-crystal sapphire and a polycrystalline Al_2O_3 material, showing the R1 and R2 "ruby" lines and the shift of these lines in the polycrystalline material due to residual stress, temperature, and compositional changes. For easy comparison the polycrystalline Al_2O_3 spectrum has been reduced to 75% intensity.

The base equation for the change in energy with stress, σ_{ij}, of fluorescence lines in the Al_2O_3 corundum structure is [21]

$$\Delta\nu = \Pi_{11}\sigma_{11} + \Pi_{22}\sigma_{22} + \Pi_{33}\sigma_{33}, \tag{2}$$

where the tensor axes (1, 2, 3) correspond to the corundum crystallographic axes (*a*, *m*, *c*). The Π_{ij} terms are the piezospectroscopic coefficients and in corundum only those given in Eq. (2) are non-zero. In principal, the three-fold rotational symmetry about the corundum *c* axis should lead to equivalence of the *a* and *m* axes, and this is what is assumed here, using conventional notation of $\Pi_{11} = \Pi_{22} = \Pi_a$ and $\Pi_{33} = \Pi_c$. Π_a and Π_c are different for the R1 and R2 fluorescence lines such that there are four coefficients of interest: $\Pi_a^{(1)}$, $\Pi_c^{(1)}$, $\Pi_a^{(2)}$, and $\Pi_c^{(2)}$. Under hydrostatic conditions, $\sigma_{11} = \sigma_{22} = \sigma_{33} = -p$, where *p* is the pressure, and thus

$$\Delta\nu^{(1)} = -\left(2\Pi_a^{(1)} + \Pi_c^{(1)}\right)p \tag{3a}$$

$$\Delta\nu^{(2)} = -\left(2\Pi_a^{(2)} + \Pi_c^{(2)}\right)p. \tag{3b}$$

Measurements of the piezospectroscopic coefficients show that the pressure coefficients are equal, $2\Pi_a^{(1)} + \Pi_c^{(1)} = 2\Pi_a^{(2)} + \Pi_c^{(2)}$ [22,23], and thus under purely hydrostatic conditions $\Delta\nu^{(1)} = \Delta\nu^{(2)}$. In fact, this condition is now taken as an indication of pure hydrostatic (*i.e.*, zero shear) loading in high-pressure diamond anvil cell experiments that make use of Eqs. (3a) and (3b) in determining pressure [24]. At high pressures (*e.g.*, greater than several gigapascals), the coefficients vary considerably with pressure; for the small stresses considered here the Π values are constant.

Eq. (2) can be re-arranged to give [21,25,26]

$$\begin{aligned}\Delta\nu &= (2\Pi_a + \Pi_c)(\sigma_{11} + \sigma_{22} + \sigma_{33})/3 + (\Pi_c - \Pi_a)(2\sigma_{33} - \sigma_{11} - \sigma_{22})/3 \\ &= (2\Pi_a + \Pi_c)\sigma_M + (\Pi_c - \Pi_a)\sigma_S\end{aligned} \tag{4}$$

where the second line in Eq. (4) generalizes Eqs. (3a) and (3b) and emphasizes that the first term provides a contribution to the shift from the local mean stress in the structure, σ_M, and the second term provides a contribution from a local shear stress, σ_S:

$$\sigma_M = (\sigma_{11} + \sigma_{22} + \sigma_{33})/3 \tag{5a}$$

$$\sigma_S = (2\sigma_{33} - \sigma_{11} - \sigma_{22})/3. \tag{5b}$$

Writing

$$\Pi_M = (2\Pi_a + \Pi_c) \tag{6a}$$

$$\Pi_S = (\Pi_c - \Pi_a), \tag{6b}$$

enables Eq. (4) to be written compactly in matrix form for each fluorescence line as

$$\begin{bmatrix}\Delta\nu^{(1)} \\ \Delta\nu^{(2)}\end{bmatrix} = \begin{bmatrix}\Pi_M^{(1)} & \Pi_S^{(1)} \\ \Pi_M^{(2)} & \Pi_S^{(2)}\end{bmatrix}\begin{bmatrix}\sigma_M \\ \sigma_S\end{bmatrix}. \tag{7}$$

Eq. (7) is easily inverted to give

$$\begin{bmatrix}\sigma_M \\ \sigma_S\end{bmatrix} = \Pi_M^{(1)}\Pi_S^{(2)} - \Pi_S^{(1)}\Pi_M^{(2)^{-1}}\begin{bmatrix}\Pi_S^{(2)} & -\Pi_S^{(1)} \\ -\Pi_M^{(2)} & \Pi_M^{(1)}\end{bmatrix}\begin{bmatrix}\Delta\nu^{(1)} \\ \Delta\nu^{(2)}\end{bmatrix}, \tag{8}$$

which allows two components of the stress field (σ_M, σ_S) to be determined from the two shift measurements ($\Delta\nu^{(1)}$, $\Delta\nu^{(2)}$).

Eq. (8) provides the basis for fluorescence-based residual stress mapping in polycrystalline Al_2O_3 with no assumptions regarding the nature of the stress field at a point in the map or the distribution of stresses over the map. However, if the multiple $\Delta\nu^{(1)}$ and $\Delta\nu^{(2)}$ values obtained in a map are averaged to obtain the mean values $\overline{\Delta\nu}^{(1)}$ and $\overline{\Delta\nu}^{(2)}$, Eq. (8) then relates these latter values to the means of the spherical and shear stresses in the structure, $\overline{\sigma}_M$ and $\overline{\sigma}_S$ respectively, by

$$\begin{bmatrix}\overline{\sigma}_M \\ \overline{\sigma}_S\end{bmatrix} = \Pi_M^{(1)}\Pi_S^{(2)} - \Pi_S^{(1)}\Pi_M^{(2)^{-1}}\begin{bmatrix}\Pi_S^{(2)} & -\Pi_S^{(1)} \\ -\Pi_M^{(2)} & \Pi_M^{(1)}\end{bmatrix}\begin{bmatrix}\overline{\Delta\nu}^{(1)} \\ \overline{\Delta\nu}^{(2)}\end{bmatrix}. \tag{9}$$

Eq. (9) provides a method for assessing the validity of the fluorescence-based mapping methodology by enabling a direct experimental test of the equilibrium condition $\overline{\sigma}_M = 0$.

Alternatively, Eq. (2) can be used to relate the mean shift values $\overline{\Delta\nu}^{(1)}$ and $\overline{\Delta\nu}^{(2)}$ to the mean crystallographic stresses in the structure, $\overline{\sigma}_a$ and $\overline{\sigma}_c$, by

$$\begin{bmatrix}\overline{\Delta\nu}^{(1)} \\ \overline{\Delta\nu}^{(2)}\end{bmatrix} = \begin{bmatrix}2\Pi_a^{(1)} & \Pi_c^{(1)} \\ 2\Pi_a^{(2)} & \Pi_c^{(2)}\end{bmatrix}\begin{bmatrix}\overline{\sigma}_a \\ \overline{\sigma}_c\end{bmatrix}. \tag{10}$$

Eq. (10) is easily inverted to give

$$\begin{bmatrix}\overline{\sigma}_a \\ \overline{\sigma}_c\end{bmatrix} = \left(2\Pi_a^{(1)}\Pi_c^{(2)} - 2\Pi_a^{(2)}\Pi_c^{(1)}\right)^{-1}\begin{bmatrix}\Pi_c^{(2)} & -\Pi_c^{(1)} \\ -2\Pi_a^{(2)} & 2\Pi_a^{(1)}\end{bmatrix}\begin{bmatrix}\overline{\Delta\nu}^{(1)} \\ \overline{\Delta\nu}^{(2)}\end{bmatrix}, \tag{11}$$

which allows the two mean components of the stress field in the crystallographic coordinates ($\overline{\sigma}_a$, $\overline{\sigma}_c$) to be determined from the two mean shift measurements ($\overline{\Delta\nu}^{(1)}$,$\overline{\Delta\nu}^{(2)}$). Eq. (11) also provides a method for assessing the validity of the methodology by enabling a direct experimental test of the equilibrium condition $\overline{\sigma}_c/\overline{\sigma}_a = -2$.

If the stress field is equibiaxial in the corundum basal plane, $\sigma_{11} = \sigma_{22} = \sigma_a$, with a different stress out of the plane, $\sigma_{33} = \sigma_c$, the constraint that Eqs. (10) and (11) relate *mean* shifts and stresses is lifted, resulting in [27]

$$\begin{bmatrix}\Delta\nu^{(1)} \\ \Delta\nu^{(2)}\end{bmatrix} = \begin{bmatrix}2\Pi_a^{(1)} & \Pi_c^{(1)} \\ 2\Pi_a^{(2)} & \Pi_c^{(2)}\end{bmatrix}\begin{bmatrix}\sigma_a \\ \sigma_c\end{bmatrix} \tag{12}$$

and thus

$$\begin{bmatrix}\sigma_a \\ \sigma_c\end{bmatrix} = \left(2\Pi_a^{(1)}\Pi_c^{(2)} - 2\Pi_a^{(2)}\Pi_c^{(1)}\right)^{-1}\begin{bmatrix}\Pi_c^{(2)} & -\Pi_c^{(1)} \\ -2\Pi_a^{(2)} & 2\Pi_a^{(1)}\end{bmatrix}\begin{bmatrix}\Delta\nu^{(1)} \\ \Delta\nu^{(2)}\end{bmatrix}. \tag{13}$$

Eq. (13) allows two components of the stress field (σ_a, σ_c) in the crystallographic coordinates to be determined from the two shift measurements ($\Delta\nu^{(1)}$, $\Delta\nu^{(2)}$) and can be applied locally to map stresses in the same way as Eq. (8), providing the stress field is known or assumed to be transversely isotropic in the *a*–*c* coordinates. Eq. (13) applies exactly in the case of a *c*-axis single crystal fiber in a matrix [27–30], or in a *c*-axis single-crystal or *c*-axis aligned mosaic polycrystalline-film on a restraining substrate, or between two restraining layers [31]. In the case of an unaligned polycrystal, Eq. (13) provides a basis for residual stress mapping with the assumption that the CTE-induced residual stress field at a point within a grain is well-approximated by the transversely isotropic field described by Eq. (12). The linearity of Eqs. (10)–(13) implies that averaged over a large number of points in such a map, the mean σ_a and σ_c values inferred from the transversely isotropic stress approximation and the use of Eq. (13) converge to the $\overline{\sigma}_a$ and $\overline{\sigma}_c$ values of Eq. (11), such that the mean values agree independent of the approximation. Note that none of the above equations implies that the off-diagonal tensor shear-stress components, σ_{12}, $_{13}$, and σ_{23} are zero; fluorescence shift measurements are simply insensitive to these

components. In fact, if there are spatial variations in on-diagonal (σ_M, σ_S) or (σ_a, σ_c) components, mechanical equilibrium requires the shear components to be non-zero. Note also that neither Eq. (8) nor Eq. (13) makes any assumptions regarding the probability distributions of stress components within the polycrystal.

2.2. Stress optical analysis for large-area scans

In a large area scan, an integrated intensity variation with wavenumber, $I_A(\nu)$, is measured:

$$I_A(\nu) = \frac{1}{A}\int_A I_{xy}(\nu)\mathrm{d}x\mathrm{d}y, \tag{14}$$

where the integral is over the scanned area A and $I_{xy}(\nu)$ is the intensity spectrum arising from location (x,y) within A. For a reference material $I_A(\nu) = I_0(\nu)$ and the reference peak position ν_0 is given by the first moment of the reference spectrum [3]:

$$\nu_0 = \int I_0(\nu)\nu\mathrm{d}\nu, \tag{15}$$

where the integral is over the measured wavenumber range encompassing the peak and a normalization of $\int I_0\nu\mathrm{d}\nu = 1$ is assumed for each R1 and R2 peak. The dispersion of the reference intensity is given by the second moment of the reference spectrum:

$$\langle\nu^2\rangle_0 = \int I_0(\nu)(\nu-\nu_0)^2\mathrm{d}\nu. \tag{16}$$

For a *single crystal* reference material as used here, $I_0(\nu)$ and thus ν_0 and $\langle\nu^2\rangle_0$ do not depend on the location of the measurement on the material or the scale of A.

For a polycrystalline material, the mean peak position in a large area scan, ν_A, is given by

$$\nu_A = \int I_A(\nu)\nu\mathrm{d}\nu, \tag{17}$$

where $\int I_A(\nu)\mathrm{d}\nu = 1$ is assumed. The mean peak shift in the polycrystalline material is then given by a modification of Eqs. (1a) and (1b):

$$\overline{\Delta\nu}_A = \nu_A - \nu_0 - \overline{\Delta\nu}_T - \overline{\Delta\nu}_C, \tag{18}$$

where $\overline{\Delta\nu}_T$ and $\overline{\Delta\nu}_C$ are the average shifts in line position associated with variations in temperature and composition over the large area scan. Note that the mean peak shifts determined in this way from a large area scan are intensity weighted via Eqs. (14), (15), and (17), in distinction to those obtained from a map, appearing in Eqs. (9)–(11), that are not intensity weighted. The dispersion of the polycrystalline large area scan is given by

$$\langle\nu^2\rangle_A = \int I_A(\nu)(\nu-\nu_A)^2\mathrm{d}\nu, \tag{19}$$

such that the change in dispersion is given by

$$\langle\Delta\nu^2\rangle = \langle\nu^2\rangle_A - \langle\nu^2\rangle_0. \tag{20}$$

The change in dispersion determined from a large area scan is also intensity weighted via Eqs. (14)–(19), again in distinction to any measure of dispersion obtained from a map that would not be intensity weighted. In addition, Eq. (20) characterizes the change in dispersion of a single integrated or convoluted peak via Eq. (14) [3] rather than that for a distribution of multiple values obtained from a map reflected in Eqs. (9) and (11). This difference is considered in [19]. Often Eqs. (15) and (17) are not used to determine ν_0 and ν_A but the raw spectra are fit to an assumed functional form (*e.g.*, Lorentzian, Lorentzian-Gaussian mixture, or Pearson) to obtain peak centroids; or the mode wavenumber is used. Similarly, Eqs. (16) and (19) are often not used to obtain $\langle\nu^2\rangle_0$ and $\langle\nu^2\rangle_A$but the half-width at half-height (HWHH) of the raw spectra is taken as a measure of dispersion. These different analysis methods do not lead to significantly different parameter estimates, especially for reference materials.

Most often in large area scan measurements, the R1 and R2 peaks are not used jointly to provide separate determinations of two stress components as shown in Eqs. (7)–(13) above. Instead, the mean shift of single peak, determined using Eq. (18), along with Eq. (2), is used to relate the shift to the mean crystallographic stresses sensed in the large area scan:

$$\overline{\Delta\nu}_A = 2\Pi_a\overline{\sigma}_a + \Pi_c\overline{\sigma}_c. \tag{21}$$

If the equilibrium condition $\overline{\sigma}_c = -2\overline{\sigma}_a$ is now imposed, Eq. (21) can be inverted to give for each fluorescence line

$$\overline{\sigma}_c = -2\overline{\sigma}_a = \overline{\Delta\nu}_A/(\Pi_c - \Pi_a) \tag{22}$$

and provide a measurement of the mean crystallographic stresses [3, 32]. The distributions of stresses about these mean values can be determined from the change in dispersion, Eq. (20), if the stresses are regarded as independent and Gaussian distributions with the same variance, σ_w^2, are assumed in both crystallographic directions [3]. The probability density functions for σ_a and σ_c are then given by

$$\mathrm{dPr}(\sigma_a)/d\sigma_a = \left(2\pi\sigma_w^2\right)^{-1/2}\exp\left[-(\sigma_a-\overline{\sigma}_a)^2/2\sigma_w^2\right] \tag{23a}$$

$$\mathrm{dPr}(\sigma_c)/d\sigma_c = \left(2\pi\sigma_w^2\right)^{-1/2}\exp\left[-(\sigma_c-\overline{\sigma}_c)^2/2\sigma_w^2\right]. \tag{23b}$$

The variance of the stress distributions is related to the change in dispersion, $\langle\Delta\nu^2\rangle$, by

$$\sigma_w^2 = \langle\Delta\nu^2\rangle/\left(4\Pi_a^2 + \Pi_c^2\right) \tag{24}$$

for each fluorescence line [3].

2.3. Stress, temperature, and composition coefficients

The piezospectroscopic coefficients used here are those of He and Clarke [23,33] modified in a minor way to be consistent with the measurements of R1 and R2 shifts as a function of hydrostatic pressure and temperature by Munro et al. [22], which, in turn, are consistent with recent measurements and review of the pressure coefficient as a function of pressure by Chijioke et al. [24]. The values are $\Pi_a^{(1)} = 3.03\ \mathrm{cm}^{-1}/\mathrm{GPa}$, $\Pi_c^{(1)} = 1.53\ \mathrm{cm}^{-1}/\mathrm{GPa}$, $\Pi_a^{(2)} = 2.73\ \mathrm{cm}^{-1}/\mathrm{GPa}$, and $\Pi_c^{(2)} = 2.16\ \mathrm{cm}^{-1}/\mathrm{GPa}$. The values for $\Pi_c^{(1)}$, $\Pi_a^{(2)}$, and $\Pi_c^{(2)}$ are unaltered from those of [33]; the value of $\Pi_a^{(1)}$ has been reduced slightly from that in [33] so that for both R1 and R2 the pressure coefficients, $2\Pi_a^{(1)} + \Pi_c^{(1)} = 7.59\ \mathrm{cm}^{-1}/\mathrm{GPa}$ and $2\Pi_a^{(2)} + \Pi_c^{(2)} = 7.62\ \mathrm{cm}^{-1}/\mathrm{GPa}$, are consistent with the values given by Munro et al. [22]. Consideration of Eq. (8) and Eq. (13) using these piezospectroscopic coefficients shows that an uncertainty in $\Delta\nu^{(1)}$ and $\Delta\nu^{(2)}$ of $0.01\ \mathrm{cm}^{-1}$ (as will be achieved here, see below) results in a stress uncertainty of about 1.3 MPa.

Although the gross variation in the fluorescence energies and line positions with temperature is extremely non-linear [17], over the small temperature variations considered here, a few K, a linear variation is appropriate:

$$\Delta\nu_T^{(1)} = \alpha_T^{(1)}(T-298.8) \tag{25a}$$

$$\Delta\nu_T^{(2)} = \alpha_T^{(2)}(T-298.8), \tag{25b}$$

where T is the temperature in K. The temperature coefficients used were those given by Munro et al. [22]: $\alpha_T^{(1)} = -0.130\ \mathrm{cm}^{-1}/\mathrm{K}$ and $\alpha_T^{(2)} = -0.122\ \mathrm{cm}^{-1}/\mathrm{K}$. Consideration of Eqs. (25a) and (25b) using these temperature coefficients shows that an uncertainty in T of 0.1 K (as here) results in a wavenumber temperature correction of $0.013\ \mathrm{cm}^{-1}$, which translates into an equivalent stress uncertainty of about 1.7 MPa.

Heavily Cr-doped ruby exhibits large non-linear changes in spectral behavior with composition as electronic interaction effects between neighboring Cr ions are significant [34]. This is not the case here for lightly doped (<0.5% Cr) polycrystalline material in which such interaction effects are expected to be insignificant. The variation of shift with composition is thus taken as linear, reflecting only the small difference in size between Cr and Al [20]:

$$\Delta\nu_C^{(1)} = \beta_C^{(1)} C_m \tag{26a}$$

$$\Delta\nu_C^{(2)} = \beta_C^{(2)} C_m, \tag{26b}$$

where C_m is the mass fraction of Cr in the Al_2O_3:Cr structure. The composition coefficients used were those determined below, $\beta_C^{(1)} = 160\ \mathrm{cm}^{-1}$ and $\beta_C^{(2)} = 167\ \mathrm{cm}^{-1}$. Consideration of Eqs. (26a) and (26b) using these composition coefficients shows that a change in C_m of 10^{-4} (about half of that here) results in a wavenumber composition correction of $0.017\ \mathrm{cm}^{-1}$, which translates into an equivalent stress change of about 2.2 MPa.

2.4. Microcrack fracture mechanics

Once obtained, the spatial variation of stress contained in a map can be used in fracture mechanics calculations for design considerations. The example application considered here is the driving force for spontaneous microcracking, in which the driving force will be characterized by the stress-intensity factor, K_μ, arising from the CTE-driven microstructural interactions.

For an assumed straight crack of length c propagating in the x direction, the stress-intensity factor is given by [35]

$$K = 2(c/\pi)^{1/2} \int_0^c \left[\sigma(x)/\left(c^2 - x^2\right)^{1/2}\right] \mathrm{d}x, \tag{27}$$

where $\sigma(x)$ is the stress distribution acting over the crack. It is easy to show that if $\sigma(x) = \sigma_R$, a constant, that $K = \pi^{1/2}\sigma_R c^{1/2}$, and this is the approximation made earlier in consideration of residual stress effects for short cracks in Al_2O_3 [12]. For the example application here, the stress distribution $\sigma_M(s)$ will be used, taken to be the variation of σ_M along a straight line path in the microstructure quantified by coordinate s, leading to

$$K_\mu = 2(c/\pi)^{1/2} \int_0^c \left[\sigma_M(s)/\left(c^2 - s^2\right)^{1/2}\right] \mathrm{d}s. \tag{28}$$

Eq. (28) assumes that the crack path is negligibly perturbed from straight by shear stress, elastic modulus, or fracture resistance variations along the path and that $\sigma_M(s)$ is a good approximation to the maximum principal stress variation along the path. Both of these assumptions are often obviously not so in polycrystalline Al_2O_3 [11,14–16], but for the purposes of illustrating the power of mapping in design considerations, Eq. (28) is adequate [12]. $K_\mu(c)$ will be obtained by simple numerical integration of Eq. (28).

3. Experimental methods

3.1. Materials

Two Al_2O_3 single-crystals were taken as stress-free reference materials as in a previous study [19]. The first was Standard Reference Material 1990 (NIST, Gaithersburg, MD), in the form of single-crystal ruby spheres, 152 μm in diameter with a Cr content of 0.428% expressed as a mass fraction of Cr in Al_2O_3:Cr. The second reference material was a single-crystal sapphire plate, 12.5 mm × 12.5 mm square × 0.5 mm thick, with c axis oriented perpendicular to the square face and Al_2O_3 purity > 99.99% as stated by the supplier (MTI, Richmond, CA). X-ray diffraction measurements of the ruby and sapphire gave identical basal plane lattice spacing within relative experimental uncertainty of 3×10^{-4}, consistent with no significant internal stress field difference between the single crystals.

A polycrystalline Al_2O_3 material was considered in detail for quantitative stress mapping. The material was one of a series of three materials studied extensively in a previous work [36] considering fracture properties of Al_2O_3, and then subsequently studied in the previous fluorescence-based stress mapping study [19]. Processing and microstructural details are given elsewhere [36], but in brief: The material was infused in a porous state with a chromate solution prior to sintering for 12 h at 1600 °C in H_2. The resulting polycrystalline material had greater than 99.5% relative density and the mode grain size was approximately 15 μm, although the grain-size distribution was broad and some grains were as large as 60 μm. After sintering, the Cr-infused material was translucent and pinkish in color. Sections of samples were polished for electron microprobe analysis, which showed a Cr content of approximately 0.025% expressed as the mass fraction of Cr in Al_2O_3:Cr. Another section of material was cut and polished for hyperspectral fluorescence microscopy.

3.2. Hyperspectral scanning fluorescence microscopy

The confocal sample-scanning optical microscope was based on a custom-built design previously described [19,37] with the following modifications: Excitation was accomplished with an optically pumped semiconductor laser operating at 488 nm. The light was spatially filtered and transported to the microscope via a single mode optical fiber. Light was coupled out of the fiber through a reflective collimator (Thorlabs, Newton, NJ) and spectrally filtered with a laser-line filter (Semrock, Rochester, NY). The linearly polarized laser light was then reflected from a long-pass edge filter (Semrock) in an inject-reject configuration onto the back aperture of a 0.75 NA, 80× air objective (ULWD MSPlan, Olympus, Center Valley, PA) that focused the light to an estimated diffraction-limited spot of radius 325 nm on the surface of the sample, which was mounted on an xyz-piezo-scan stage (NanoCube, Physik Instrumente, Karlsruhe, Germany). Epi-fluorescence from the sample was collected back through the objective, passed through the long-pass filter and focused into a multi-mode optical fiber with a 50 μm core diameter (Thorlabs) acting as the confocal aperture. It is estimated that light was collected from depths no greater than about 3 μm beneath the surface (much less than the material grain size). Note that this value is not limited by optical attenuation in the Al_2O_3 but rather by the confocal depth resolution of the microscope. The estimate of the confocal depth resolution is based on z-scan measurements on sub-micrometer optical thickness resolution artifacts. Spectra were dispersed through a 1/2-meter spectrometer (Acton SP 2500i, Princeton Instruments, Acton, MA) with a grating pitch of 2400-groove mm^{-1} and imaged on a liquid-N_2 cooled CCD camera (SPEC-10, Princeton Instruments), where the spectral region between 14,506 cm^{-1} and 14,317 cm^{-1} containing the R1 and R2 peaks was spread over the 1340 pixels of the camera (to give a pixel spacing of $\approx 0.14\ \mathrm{cm}^{-1}$). The absolute wavenumber axis for the camera was calibrated using five atomic emission reference lines that occur in this spectral range from neon, argon, and krypton

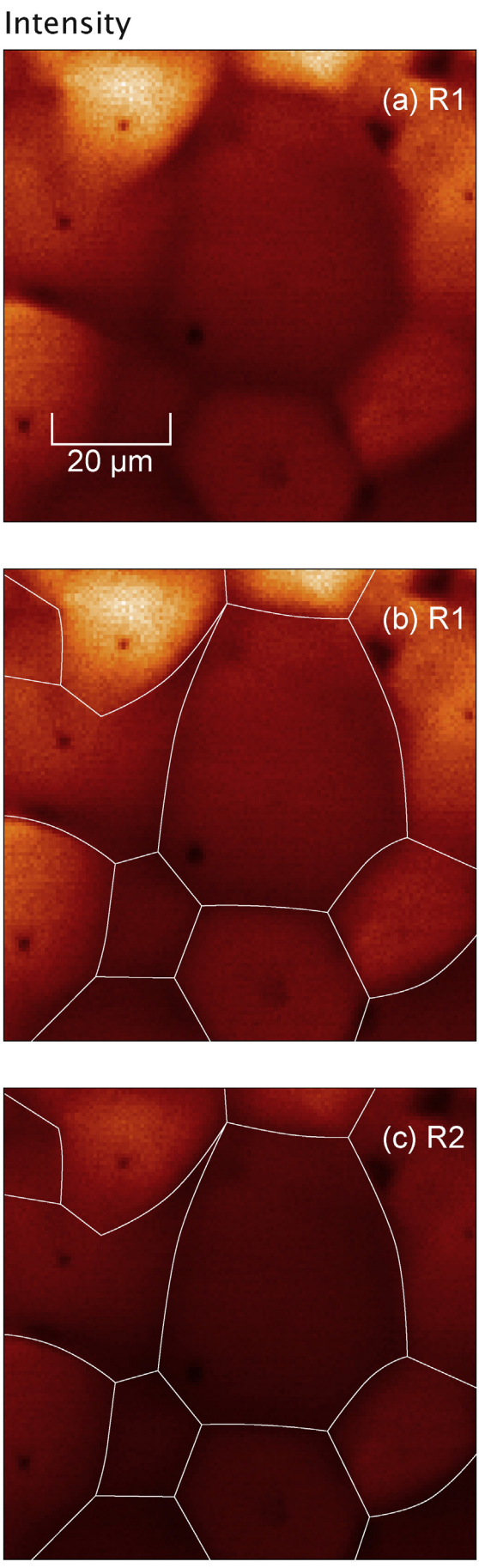

lamps. A thermistor mounted on the sample holder was used to record the temperature prior to acquisition of each individual spectrum in both the reference material spectral acquisition sequences and in the hyperspectral maps described in the following section. This temperature was then used to calculate corrected spectral line shifts at 298.8 K as described in Eqs. (25a) and (25b).

3.3. Reference calibration and hyperspectral mapping

Repeat fluorescence spectra from the same sample location were obtained for the two single-crystal reference materials. Forty-nine spectra were collected twice for each material in two runs on separate days. The spectra from the ruby standard were collected with an incident power of 50 μW and an integration time for each spectrum of 1 s. Due to the low Cr concentration, the spectra from the sapphire crystal required 5 min integration times with an incident power of 2.5 mW. The spectra were fit to a spectral model consisting of two peaks (R1 and R2) each with a Pearson VII line shape with fixed best-fit shape parameters for each peak, yielding peak center wavenumbers, widths, and amplitudes. All peak center values were corrected to a temperature of 298.8 K using Eqs. (25a) and (25b).

A hyperspectral map of the fluorescence from the polycrystalline sample was collected from a region 80 μm × 80 μm square in 128 rows at 128 pixels per row (625 nm pixel^{-1}), integrating for 0.5 s pixel^{-1} to achieve signal-to-noise ratios >200:1. Each spectrum was fit to a dual-peak Pearson VII model with shape parameters as above, yielding peak amplitude, width, and center wavenumber parameters for R1 and R2. The peak amplitude (intensity) data were used to segment the maps into individual grains and grain-boundaries using manual image manipulation, taking advantage of the strong polarization dependence of the fluorescence intensity [33] and the different orientations of individual grains relative to the excitation polarization. All peak center values were corrected to a temperature of 298.8 K using Eqs. (25a) and (25b) and composition shift factors calculated using Eqs. (26a) and (26b). The polycrystalline peak center data were used in combination with the single-crystal sapphire control measurements and the temperature and composition shift factors to determine peak center shifts associated solely with stress effects as in Eqs. (1a) and (1b), and were analyzed as described above in Section 2.1.

Individual spectra from each point in the polycrystalline map were summed and then divided by the number of spectra to form an effective integrated large-area scan spectrum in the manner of Eq. (14). No temperature corrections were applied in the spectral summation and average. Peak and width characteristics of this single spectrum were used in combination with those of the single crystal sapphire control measurements, the average temperature during the map, and temperature and composition shift factors to determine peak center shift and change in dispersion as in Eqs. (18) and (20), and were analyzed as described in Section 2.2.

4. Results

4.1. Single crystal reference measurements

Fig. 1 shows a single representative spectrum obtained from the single-crystal sapphire specimen. Analysis of all 98 repeat measurements of the sapphire gave mean R1 and R2 peak center positions adjusted to 298.8 K of (14,402.83 ± 0.01) cm^{-1} and (14,432.64 ± 0.01) cm^{-1}, respectively (where the uncertainties here and throughout, unless otherwise noted, represent standard deviations of experimental quantities,

Fig. 2. (a) Intensity map of R1 fluorescence peak in a polycrystalline Al_2O_3; fluorescence polarization effects provide a contrast mechanism for the differently-oriented grains. (b) Same map as (a) with grain boundaries overlaid. (c) Intensity map of R2 fluorescence peak over the same region and using the same intensity scale as (a) with the grain boundaries from (b) overlaid. R2 is less intense than R1.

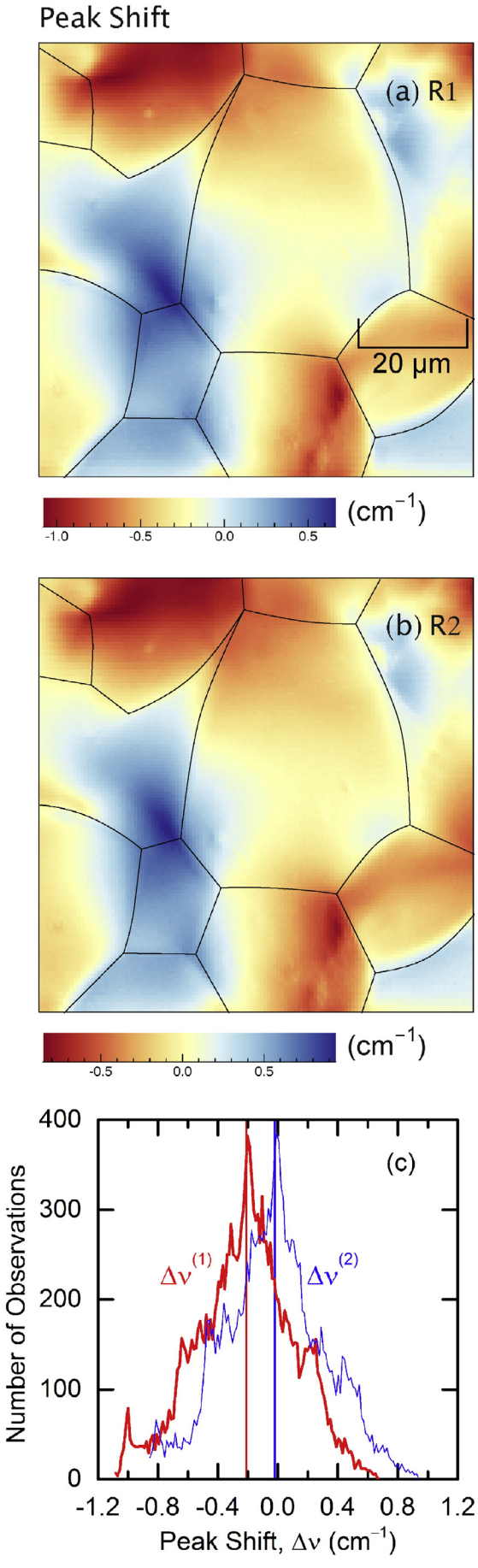

i.e., Type 1 uncertainties). These values will be taken as $\nu_0^{(1)}$ and $\nu_0^{(2)}$, respectively, in Eqs. (1a), (1b) and (15) and are consistent with (14,402.5 ± 0.4) cm^{-1} and (14,432.1 ± 0.4) cm^{-1} reported by Munro et al. [22] (where here the uncertainties represent 99% confidence bounds including Type 1 and Type 2 uncertainties). The average HWHH values for the sapphire peaks were, as previously [20], 5.50 cm^{-1} and 4.43 cm^{-1} for R1 and R2, respectively. These values will be taken as $[\langle\nu^2\rangle_0^{(1)}]^{1/2}$ and $[\langle\nu^2\rangle_0^{(2)}]^{1/2}$ in Eq. (20).

The spectra from the ruby single crystal were much greater in intensity than the sapphire spectra, reflecting the much greater Cr content. Based on the relative spectral amplitudes, Cr content in the sapphire specimen was estimated to be about 1×10^{-5} mass fraction. For both R1 and R2, the center positions of the ruby peaks were shifted to greater wavenumbers compared with those for the sapphire peaks: R1 and R2 peak center positions adjusted to 298.8 K were (14,403.513 ± 0.006) cm^{-1} and (14,433.355 ± 0.006) cm^{-1}, respectively. Assuming shift differences deriving solely from the substantial Cr composition of the ruby relative to the negligible Cr composition of the sapphire, the ruby–sapphire peak-center shift differences determined here are (0.68 ± 0.01) cm^{-1} for R1 and (0.72 ± 0.01) cm^{-1} for R2, where the uncertainties were determined by propagation of variance. These values are taken as $\Delta\nu_C^{(1)}$ and $\Delta\nu_C^{(2)}$ in Eqs. (1a) and (1b). Using the composition of the ruby gives values of $\beta_C^{(1)} = 160$ cm^{-1} and $\beta_C^{(2)} = 167$ cm^{-1} in Eqs. (26a) and (26b), slightly greater than those determined previously [19].

4.2. Polycrystalline material stress maps

Fig. 2(a) is a map of the R1 peak intensity for the polycrystalline material. The fluorescence intensity is strongly polarization dependent and thus the differently-oriented grains relative to the polarization of the laser excitation exhibit strong contrast and the microstructure is clearly apparent. Fig. 2(b) is the same map as Fig. 2(a) with grain boundaries indicated as a guide to the eye by solid lines. The boundary positions were determined visually using the intensity contrast in the image of Fig. 2(a) and manually drawn. (For a single clear image as in Fig. 2(a), the quasi-automated digital image analysis used previously to segment many images [19] was not necessary.) Fig. 2(c) is a map of the R2 peak intensity over the same region as Fig. 2(a) using the same intensity scale and with the grain boundaries identified in Fig. 2(b) superimposed. It is clear that the R2 peak intensity is less than that of the R1 peak intensity, consistent with Fig. 1 and previous observations [3,18,19] and that the two peak intensities are strongly correlated on a grain by grain basis, such that either could be used to segment the microstructure.

Fig. 3(a) and (b) are maps of the stress-related R1 and R2 peak shifts, $\Delta\nu^{(1)}$ and $\Delta\nu^{(2)}$, determined from analysis of the raw hyperspectral measurements of the polycrystalline material over the same region as Fig. 2, and using the reference material measurements and temperature and composition correction factors as given above in Eqs. (1a) and (1b). The grain boundaries as determined in Fig. 2 are superimposed. Note the change in scale for R1 and R2. There is a strong correlation between shift and microstructure, with small variations in shift within grains and greatest gradients in shift occurring at grain boundaries. There is also strong correlation between the R1 and R2 shifts. These correlations between shift and microstructure are consistent with those made previously [19], in which R1 shift maps alone were used. The differences between the R1 and R2 shift are made clear in Fig. 3(c), which shows histograms of the R1 and R2 shift distributions from the maps in Figs. 3(a) and (b) (16384 observations spread over 128 bins). Although the range of shifts observed for R1 and R2 are similar (about 1.8 cm^{-1}), the

Fig. 3. Maps of (a) R1 and (b) R2 stress-driven fluorescence peak shifts in polycrystalline Al_2O_3. The grain boundaries identified in the R1 intensity map of Fig. 2(b) are overlaid. (c) Histograms of the observed peak shifts for R1 and R2; the vertical lines indicate the mean shifts of the histograms.

shift magnitudes are smaller for R2 than R1. The solid vertical lines in Fig. 3(c) indicate the mean values of the shift distributions, $\overline{\Delta\nu}^{(1)}$ and $\overline{\Delta\nu}^{(2)}$; the values are given in Table 1.

Fig. 4(a) and (b) are maps of the local mean and shear stresses, σ_M and σ_S, determined from the shifts in Fig. 3 and Eq. (8). The grain boundaries as determined in Fig. 2 are superimposed and the scale is different for σ_M and σ_S. There is a strong correlation between the state of stress and the grain structure, particularly for σ_S. Fig. 4(c) shows histograms of the σ_M and σ_S stress distributions from the maps of Fig. 4(a) and (b). The mean stress values, $\overline{\sigma}_M$ and $\overline{\sigma}_S$, calculated from the mean shift values and Eq. (9), are indicated in Fig. 4(c) by vertical lines; the values are given in Table 1 along with the standard deviations of the distributions of σ_M and σ_S from the maps.

Fig. 5(a) and (b) are maps of the two components of the stress field in the crystallographic coordinates, σ_a and σ_c, determined from the shifts in Fig. 3 and Eq. (13). The grain boundaries as determined in Fig. 2 are superimposed and the scale is different for σ_a and σ_c. There is a strong correlation between the state of stress and the grain structure, particularly for σ_c. Fig. 5(c) shows histograms of the σ_a and σ_c stress distributions from the maps of Fig. 5(a) and (b); the histogram for σ_a has been plotted with doubled amplitude to be consistent with the equilibrium condition,

$$\int 2F_a(\sigma_a)\sigma_a d\sigma_a + \int F_c(\sigma_c)\sigma_c d\sigma_c = 0, \tag{29}$$

where $F(\sigma)$ is a histogram. The mean stress values, $\overline{\sigma}_a$ and $\overline{\sigma}_c$, calculated from the mean shift values and Eq. (11), are indicated in Fig. 5(c) by vertical lines; the values are given in Table 1 along with the standard deviations of the distributions of σ_a and σ_c from the maps.

4.3. Polycrystalline material large area scan

Fig. 6 shows the effective integrated large-area scan spectrum for the polycrystalline Al_2O_3 material calculated from the complete set of hyperspectral data giving rise to Figs. 2 and 3. For comparison, the single pixel polycrystalline Al_2O_3 spectrum shown in Fig. 1 is repeated; the integrated spectrum in Fig. 6 is the (intensity-weighted) average of $(128 \times 128 = 16{,}384)$ such spectra. Fits to the R1 and R2 peak positions of the integrated spectrum gave mean peak positions of $\nu_A^{(1)} = 14{,}403.18\ \text{cm}^{-1}$ and $\nu_A^{(2)} = 14{,}433.15\ \text{cm}^{-1}$ and HWHH values of $[\langle\nu^2\rangle_A^{(1)}]^{1/2} = 5.75\ \text{cm}^{-1}$ and $[\langle\nu^2\rangle_A^{(2)}]^{1/2} = 4.62\ \text{cm}^{-1}$.

The average temperature during the generation of the integrated spectrum was 294.2 K. Using this temperature in Eqs. (25a) and (25b) to generate averaged temperature corrections, along with the reference spectra information from Section 3.1, the mean R1 and R2 stress-related shifts, $\overline{\Delta\nu}_A^{(1)}$ and $\overline{\Delta\nu}_A^{(2)}$, from the integrated spectrum were determined using Eq. (18). Using these mean shift values in Eq. (22) provides estimates of the mean crystallographic stresses $\overline{\sigma}_a$ and $\overline{\sigma}_c$ from the integrated spectrum information. Using the values of $[\langle\nu^2\rangle_A^{(1)}]^{1/2}$ and $[\langle\nu^2\rangle_A^{(2)}]^{1/2}$ and the reference spectra information in Eq. (20) enables the change in dispersion for each peak to be calculated as $[\langle\Delta\nu^2\rangle^{(1)}]^{1/2}$ and $[\langle\Delta\nu^2\rangle^{(2)}]^{1/2}$. Using these values and Eq. (24) enables the widths of the assumed Gaussian stress distributions, σ_w, to be estimated. All mean and dispersion values for shifts and stresses inferred from analysis of the integrated large area spectrum are given in Table 1.

4.4. Stress-intensity factor determination

Fig. 7(a) shows the σ_M stress map from Fig. 4(a) with two perpendicular coordinate systems OA and OB superimposed. Fig. 7(b) shows the variation of σ_M with distance s along the coordinate systems, starting with position O at which σ_M is significantly tensile; in the case of OA, the stress rapidly becomes compressive, before increasing to zero; in the case of OB, the stress increases slightly before decreasing to compressive values. Fig. 7(c) shows the stress-intensity factor K_μ calculated from these stress variations and Eq. (28) for fracture along OA and OB with crack lengths c. In both cases, the K_μ variation is a slightly concave version of the stress variation with minima and maxima shifted to greater dimensions, reflecting the weighted integration of Eq. (28).

5. Discussion and conclusions

The power of the hyperspectral fluorescence technique to generate 2-D maps of residual stress in polycrystalline Al_2O_3 is evident in Figs. 4 and 5. As implemented here, the maps demonstrate about ±1 MPa stress resolution (limited by peak position determination) and 625 nm lateral spatial resolution. The use of both the R1 and R2 fluorescence shifts increases the precision with which the stress field at a point in a map can be specified to two independent stress components. Explicit point-by-point correction for temperature variation during the mapping process, along with the use of single crystal reference materials and composition correction, enables the stresses inferred from shifts to be specified in an absolute manner, with an accuracy of about ±5 MPa (limited by peak position determination, temperature measurement, and composition). As noted in the previous brief review [19], the above specifications represent significant measurement advances on prior mapping studies, which typically used a single peak shift to specify a single stress value with about ±10 MPa stress resolution, micrometer spatial resolution at best, and no specification of accuracy.

The residual stress maps provide stress magnitudes, spatial variations, and statistical distributions, and as such can be used directly in material selection and design. Changes in Al_2O_3 processing, in particular changes in sintering time and temperature and cooling rate, can be made to design materials with specific grain sizes and grain-size distributions that give rise to specific CTE-derived residual stress fields. Such processing changes can be guided by models [2] or simulations [5–7] of residual stress that are based on equilibrium considerations of microstructural heterogeneity or models [4] of residual stress development that are based on the kinetics of stress relaxation by diffusion during cooling. As the mapping procedure here provides a measure of accuracy and hence of absolute (as opposed to relative) residual stress measurement, direct comparison with the predictions of models of residual stress, in which other absolute quantities (*e.g.*, elastic moduli, CTE coefficients, diffusivities) are used is possible. The mapping results here reinforce the agreement with model results noted earlier [19]. The key points of agreement are both quantitative (stresses of order hundreds

Table 1
Fluorescence shift and stress distribution properties of polycrystalline Al_2O_3:Cr.

	Mean R1 shift, $\overline{\Delta\nu}^{(1)}$ (cm^{-1})	Mean R2 shift, $\overline{\Delta\nu}^{(2)}$ (cm^{-1})	Mean stress, $\overline{\sigma}_M$ (MPa)	Shear stress, $\overline{\sigma}_S$ (MPa)	a-Axis stress, $\overline{\sigma}_a$ (MPa)	c-Axis stress, $\overline{\sigma}_c$ (MPa)
Mapping	−0.2101	−0.02067	12.5 ± 44.9[a]	203.3 ± 35.9[a]	−89.1 ± 42.4[a]	215.8 ± 66.2[a]
Integrated large-area	−0.2877 ± 1.68		NA	NA	−96 ± 270[b]	192 ± 270[b]
scan		−0.09326 ± 1.31	NA	NA	−82 ± 220[b]	164 ± 220[b]

[a] (Mean ± standard deviation) values of experimental distributions in maps.
[b] (Mean ± standard deviation) values from integrated spectra and assumed Gaussian distributions.

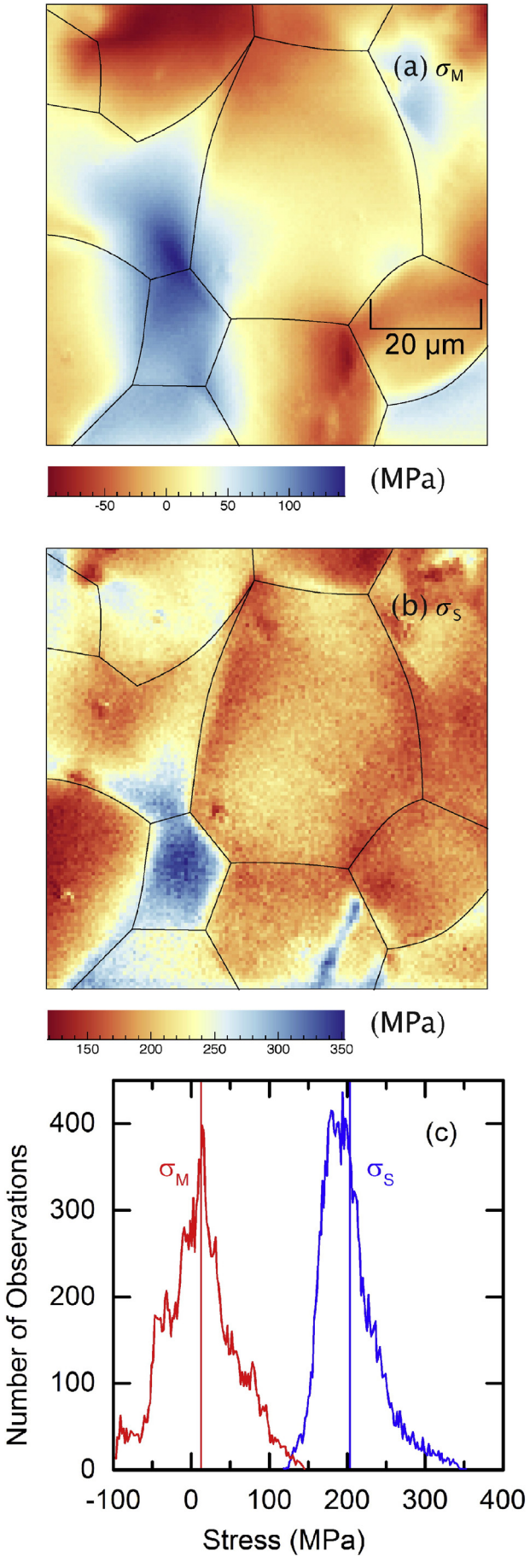

of MPa) and qualitative (stress fluctuations over length scales larger than the grain size); detailed considerations are given in [19].

As noted in the Introduction, a major reason for determining the residual stress distribution in Al_2O_3 is the effect of the stress on fracture properties. An example shown here is the calculation of stress-intensity factors for assumed crack paths in the Al_2O_3 structure, Fig. 7. For both paths OA and OB in Fig. 7, the stress is initially tensile and then becomes compressive, over length scales somewhat longer than a grain size, giving rise to a microstructural stress-intensity factor that varies with crack length, $K_\mu(c)$, that similarly fluctuates both positive and negative over similar length scales. For both paths OA and OB, $K_\mu(c)$ is considerably less than the toughness of single crystal sapphire or corundum required for transgranular fracture, about 2.5 MPa $m^{1/2}$ [11,36]. Hence, even along path OB, which exhibits a strongly positive stress-intensity factor, spontaneous transgranular microcracking is extremely unlikely. Even for intergranular fracture, spontaneous intergranular microcracking would only be possible for grain boundary toughness values of approximately 0.75 MPa $m^{1/2}$ [10], and then microcracks could only initiate and stabilize at crack lengths of approximately 20 μm. Note that fracture is more likely as the temperature is decreased [6,10], as the magnitudes of CTE-derived $\sigma_M(s)$ and $K_\mu(c)$ are increased, but that the length of the initiating and stabilized cracks does not change very much as the spatial distribution of tensile and compressive stresses is not altered by temperature (the magnitudes of both tension and compression increase with decreasing temperature). Hence, the information contained in the maps is of direct relevance in answering questions related to selection of Al_2O_3 with regard to CTE-driven microcracks: Are microcracks possible? How long are the microcracks likely to be? For longer cracks, driven by an externally-applied stress, both paths OA and OB are of interest. Path OB provides a direct assessment of the variable microstructural crack driving force at short crack lengths, rather than an assumption of uniform tension [12]. Path OA provides a direct assessment of the forces exerted by microstructural restraining elements formed in the wakes of long cracks [9,12–16], particularly those associated with discontinuous crack paths. Microstructural restraining stresses of order hundreds of MPa have been inferred from strength tests of Al_2O_3 [12,15] and by direct measurement of cracks using fluorescence point measurements [38], consistent with path OA in Fig. 7(a). Here, the maps are of relevance to questions arising in designing Al_2O_3 microstructures for specific toughness characteristics as a function of crack length: What is the possible long crack toughness? What is the trade-off between short and long crack behavior?

As also noted in the Introduction, the mapping method enables a direct assessment of the stress equilibrium conditions. To estimate the uncertainty in such an assessment for the full stress-field *population* of the material the number of degrees of freedom in the stress-field *sample* in the maps must be estimated (the number of degrees of freedom is not the number of pixels, 128×128, as the stress at a given pixel is not uncorrelated with stress at an adjacent pixel). It is noted that 12 grain regions were identified in the intensity maps of Fig. 2 and that there are about six or seven distinct stress clusters in the shift and stress maps of Figs. 3–5, suggesting that there were about nine degrees of freedom in the stress maps. As a consequence, using the sample values given in Table 1, the estimate of the population mean spherical stress is $\langle \sigma_M \rangle = (12.5 \pm 15.0)$ MPa, where $\langle\rangle$ indicates a population estimate and the uncertainty is the standard error of such an estimate (in this case $44.9/9^{1/2}$). Similarly, the estimate of the population crystallographic stress ratio is $\langle \overline{\sigma}_c/\overline{\sigma}_a \rangle = -2.42 \pm 0.46$, where the uncertainty is the standard error calculated by propagation of variance. The population estimates are not significantly different from the ideal equilibrium values of 0 and −2, validating the mapping approach and providing an upper

Fig. 4. Maps of the local (a) mean, σ_M, and (b) shear, σ_S, residual stresses determined from fluorescence mapping in polycrystalline Al_2O_3. The grain boundaries identified in the R1 intensity map of Fig. 2(b) are overlaid. (c) Histograms of the determined stresses; the vertical lines indicate the mean stresses of the histograms.

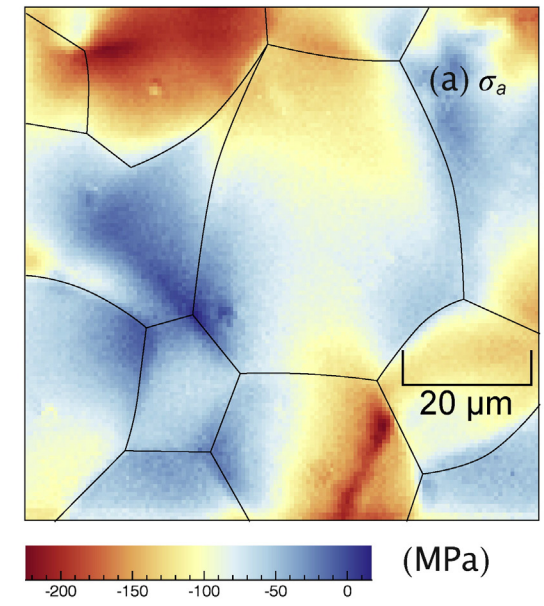

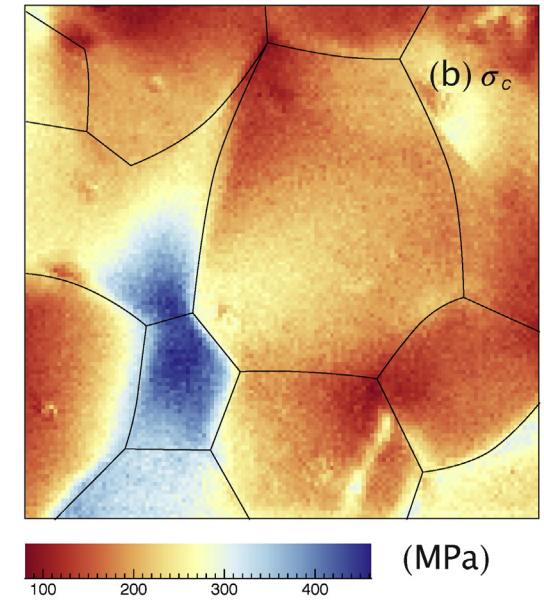

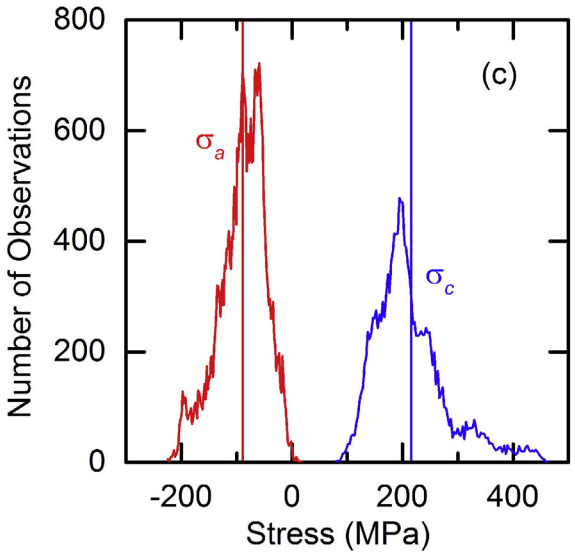

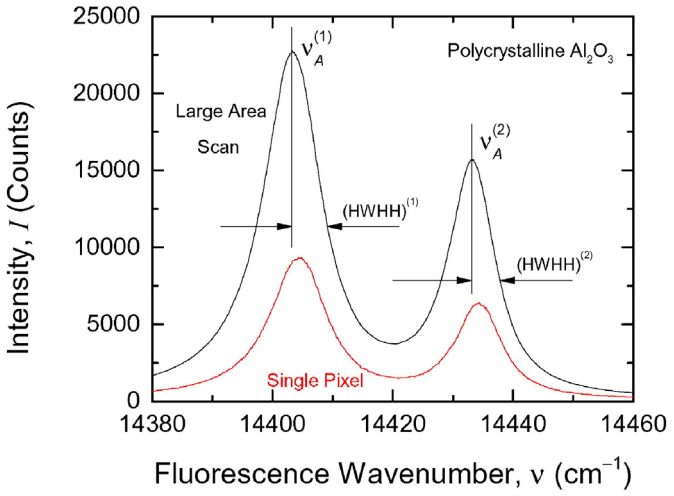

Fig. 6. An effective integrated large area scan fluorescence spectrum created from hyperspectral fluorescence mapping data for polycrystalline Al_2O_3. The integrated R1 and R2 peak center positions and half widths at half height (HWHH) are indicated. For comparison, the reduced-intensity single pixel spectrum from Fig. 1 is also shown.

bound on mapping accuracy, ±15 MPa, greater than that estimated from measurement uncertainty above. (Related to the stress ratio is the evaluation of the right side of Eq. (29), which gives a value that is similarly not significantly different from 0.) Measurements from a large number of maps and more exact analysis methods will help to refine these population estimates and provide guidance on the size of map required for a given microstructure and number of observed grains and stress clusters. This last point is emphasized in the shift and stress histograms of Figs. 3(c), 4(c), and 5(c): The histograms are asymmetric and appear to consist of several separate distributions, reflecting the shift and stress clusters observed in the maps of Figs. 3–5. The contributions of individual grains and grain boundary regions to overall stress distributions were noted in the prior study [19]. Figs. 3–5 make clear that the stress distributions are not Gaussian and that the statistics of sample maps needs to be considered in determining material population parameters.

The integrated large-area scan approach assumes that the area scanned is large enough that the equilibrium conditions are met experimentally in the scan. The assessment above suggests that this was the case here, and is consistent with the agreement between the mean values of the crystallographic stresses $\overline{\sigma}_a$ and $\overline{\sigma}_c$ estimated from integrated single-peak shifts with those estimated from maps utilizing both peak shifts (Table 1). As noted earlier [19], the dispersion in stress inferred from the integrated peak analysis, assuming Gaussian stress distributions reflected in a broadening of the integrated peak [3], greatly overestimates the width of the stress distribution measured from a map. Again, measurements from a large number of maps will enable a relationship to be established between stress dispersion determined from maps and that inferred from integrated scans. Such a relationship will put the great convenience of integrated scans on a more quantitative footing. In addition, mapping can provide confirmation that some integrated scans consist of contributions from distinct populations of stressed material, as has been assumed in studies on thermally and mechanically damaged Al_2O_3 [39–41].

For both maps and integrated scans, temperature correction was critical to generating absolute stress estimates, composition correction less so. To see this, consider the characteristic values of the

Fig. 5. Maps of the local stresses in crystallographic coordinates, (a) σ_a and (b) σ_c, determined from fluorescence mapping in polycrystalline Al_2O_3. The grain boundaries identified in the R1 intensity map of Fig. 2(b) are overlaid. (c) Histograms of the determined stresses; the vertical lines indicate the mean stresses of the histograms.

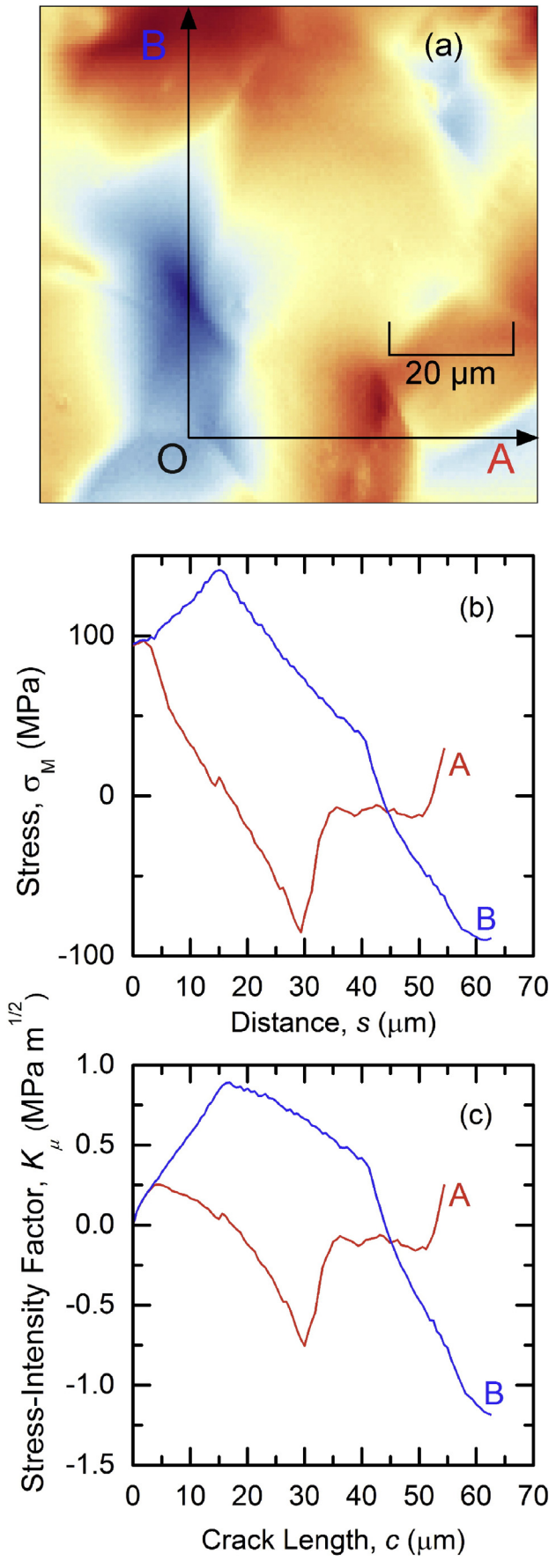

contributions to the total shift in Eqs. (1a), (1b) and (18). From Table 1, it can be seen that the stress shift, $\Delta\nu$, is the order $-0.25\ \mathrm{cm}^{-1}$ for R1 and $-0.05\ \mathrm{cm}^{-1}$ for R2. From Eqs. (25a) and (25b), using the average temperature adjustment made in the maps (-4.6 K), the temperature shift, $\Delta\nu_T$, is approximately $+0.58\ \mathrm{cm}^{-1}$ for both R1 and R2. From Eqs. (26a) and (26b), using the composition of the polycrystalline material (0.025% Cr in Al_2O_3:Cr), the composition shift, $\Delta\nu_C$, is approximately $+0.04\ \mathrm{cm}^{-1}$ for both R1 and R2. Hence, the temperature effect can be more than double the stress effect; if corrections are not made for temperature changes during mapping, the inferred stress changes would be submerged in the thermal noise and could even be interpreted as having the wrong sign. Even if there is no temperature fluctuation during mapping, no absolute estimate of stress can be made if the temperature is not known. Such inter-related temperature and stress effects have been noted in considerations of the use of ruby line shifts in high-pressure experiments [42]. Composition has a minor effect for a given material, although even here the composition correction was comparable to the R2 stress shift. For comparison between materials, composition correction is essential for absolute stress comparisons. Determinations of absolute stresses bring into consideration the absolute values and uncertainties of the Π (Eq. (2)), α (Eqs. (25a) and (25b)), and β (Eqs. (26a) and (26b)) coefficients. Variations in these quantities have not been considered in the above estimates of precision and accuracy; further comparison of maps with integrated scans and comparison of maps with independent measurements or models will require inclusion of uncertainties in these quantities into a full uncertainty budget. As noted above, constraints on these quantities and their uncertainties are provided by extensive high-pressure hydrostatic measurements.

Finally, it is useful to compare the fluorescence stress mapping technique with other techniques used to measure residual stress. In particular, as noted by Pezzotti and colleagues, stress mapping in Al_2O_3 *via* Raman spectroscopy has much in common experimentally with fluorescence stress mapping, with the significant exception that, although much diminished in intensity, corundum exhibits seven Raman lines associated with inelastic scattering of photons from lattice phonons. The shifts in these lines with stress can be calibrated to arrive at the Raman piezospectroscopic coefficients, and matrix expressions for the six independent elements of the stress or strain tensors can be written similarly to Eqs. (7) and (12) and inverted to obtain the full stress or strain tensor (with the exception that the Π_{KL} matrices are now 6×6 rather than 2×2). This has been demonstrated on polycrystalline Al_2O_3 for wear surfaces [43] (2 μm steps in 50 μm maps exhibiting a 600 MPa stress range) and thermal anisotropy residual stress [44] (1 μm steps in 80 μm maps, 1.2 GPa range), and on sapphire for indentation cracks [45] (0.1 μm steps over 12 μm line scans, 600 MPa range) and about an inclusion [46] (5 μm steps in 140 μm maps, 1.1 GPa range). Building on the polarization dependence of the Raman line intensities [47] and knowledge of the fundamental phonon deformation potentials underlying the piezospectroscopic coefficients [48], it is possible (although now at least nine variables must be measured) to use polarized Raman spectroscopy to determine the full stress or strain tensor *and* crystal orientation at a point in a map [49]. This has been demonstrated in principle (results were reported in the laboratory rather than crystallographic frame) for stress variation adjacent to a metal-polycrystalline Al_2O_3 interface [49] (μm-scale steps over a 25 μm scan, 300 MPa range). The stress ranges reported for these Raman-based studies are comparable, if somewhat greater, than those reported here from fluorescence measurements (Figs. 4 and 5), but the spatial pixel densities are considerably less, reflecting the reduced intensities and

Fig. 7. (a) Map of the local mean stress σ_M in a polycrystalline Al_2O_3 identical to that of Fig. 4(a) with two line traverses marked as solid lines OA and OB. (b) Variation of σ_M with position s over the traverses marked in (a). (c) The stress-intensity factor as a function of crack length arising from the stress variation in (b).

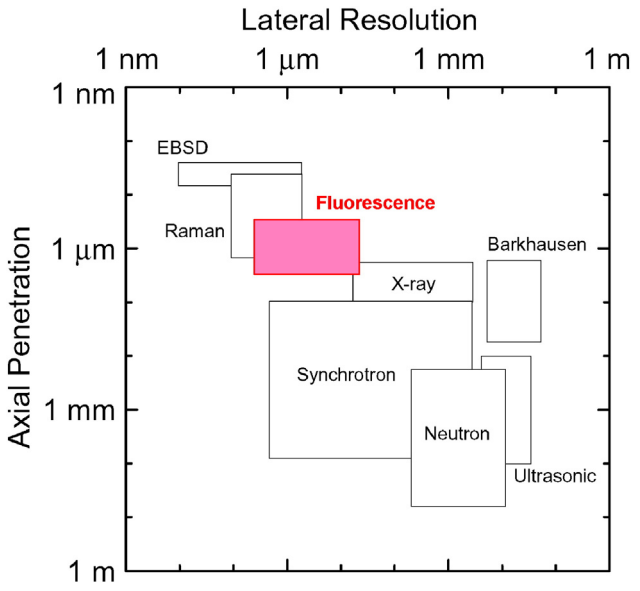

Fig. 8. Comparison of radiation-based non-destructive residual stress measurement techniques in terms of lateral resolution and axial penetration ranges (after Rossini et al. [51]).

hence required increased collection times for Raman relative to fluorescence measurements.

More broadly, in recent reviews Withers and Bhadeshia [50] and Rossini et al. [51] compared several techniques, both destructive and non-destructive, for measuring residual stresses, with emphases on structural metals and the effects of fatigue and welding. The non-destructive techniques reviewed, neutron and X-ray diffraction (including that using Synchrotron X-rays), Barkhausen resonance, and ultrasonic methods exhibited a lateral resolution range of 1 µm to 10 mm and an axial penetration range of several µm to 1 cm. At the other extreme, recent work at the near nano-scale [37,52–58] has demonstrated measurements of stress by confocal Raman microscopy and electron backscatter diffraction (EBSD) with an emphasis on microelectronic materials and structures (as opposed to the *micro*-scale Raman measurements of Al_2O_3 above [43–49]), with a lateral resolution range of 10 nm to 2 µm and an axial penetration range of 10 nm to 1.5 µm. Following Rossini et al., Fig. 8 maps the lateral resolution and axial penetration ranges for the techniques just listed, along with fluorescence microscopy presented here and earlier [20]. As can be seen, fluorescence microscopy bridges the gap between the micro- to macro-range techniques mostly applied to metals and the nano-range techniques mostly applied to semiconductors. Admittedly, fluorescence microscopy is restricted to non-metallic systems that have an appropriately stress-affected fluorescing ion, here Cr in Al_2O_3, although there are many others, including Cr in MgO, and rare-earth ions in garnets [3], but does not require the ultra-high vacuum conditions of EBSD or synchrotron measurements. Great progress has been made in assessing and improving the precision and accuracy of stress measurement by Raman microscopy and EBSD using common test vehicles in the overlapping measurement ranges [52,55,58]. Fig. 8 suggests that the best option for similar improvements in stress measurement by fluorescence microscopy is through the use of test vehicles in common with X-ray diffraction and Raman microscopy [43,46].

Acknowledgments

Certain commercial equipment, instruments, or materials are identified in this paper in order to specify the experimental procedure adequately. Such identification is not intended to imply recommendation or endorsement by the National Institute of Standards and Technology, nor is it intended to imply that the materials or equipment identified are necessarily the best available for the purpose.

References

[1] R.D. Munro, Evaluated material properties for a sintered α-alumina, J. Am. Ceram. Soc. 80 (1997) 1919–1928.
[2] W. Kreher, A. Molinari, Residual stresses in polycrystals as influenced by grain shape and texture, J. Mech. Phys. Solids 41 (1993) 1955–1977.
[3] Q. Ma, D.R. Clarke, Stress measurement in single-crystal and polycrystalline ceramics using their optical fluorescence, J. Am. Ceram. Soc. 76 (1993) 1433–1440.
[4] J.E. Blendell, R.L. Coble, Measurement of stress due to thermal expansion anisotropy in Al_2O_3, J. Am. Ceram. Soc. 65 (1982) 174–178.
[5] A. Zimmermann, E.R. Fuller Jr., J. Rödel, Residual stress distributions in ceramics, J. Am. Ceram. Soc. 82 (1999) 5155–5160.
[6] V.R. Vedula, S.J. Glass, D.M. Saylor, G.S. Rohrer, W.C. Carter, S.A. Langer, E.R. Fuller Jr., Residual-stress predictions in polycrystalline alumina, J. Am. Ceram. Soc. 84 (2001) 2947–2954.
[7] D. Gonzalez, A. King, M. Mostafavi, P. Reischig, S. Rolland du Roscoat, W. Ludwig, J. Quinta da Fonseca, P.J. Withers, T.J. Marrow, Three-dimensional observation and image-based modelling of thermal strains in polycrystalline alumina, Acta Mater. 61 (2013) 7521–7533.
[8] W.D. Kingery, H.K. Bowen, D.R. Uhlmann, Introduction to Ceramics, 2 ed. John Wiley and Sons, New York, 1976.
[9] S.J. Bennison, B.R. Lawn, Flaw tolerance in ceramics with rising crack resistance characteristics, J. Mater. Sci. 24 (1989) 3169–3175.
[10] S. Galal Yousef, J. Rödel, E.R. Fuller Jr., A. Zimmermann, B.S. El-Dasher, Microcrack evolution in alumina ceramics: experiment and simulation, J. Am. Ceram. Soc. 88 (2005) 2809–2816.
[11] R.F. Cook, B.R. Lawn, C.J. Fairbanks, Microstructure-strength properties in ceramics: I, effect of crack size on toughness, J. Am. Ceram. Soc. 68 (1985) 604–615.
[12] S.J. Bennison, B.R. Lawn, Role of interfacial grain-bridging sliding friction in the crack-resistance and strength properties of nontransforming ceramics, Acta Metall. 37 (1989) 2659–2671.
[13] R. Knehans, R. Steinbrech, Memory effect of crack resistance during slow crack growth in notched Al_2O_3 bend specimens, J. Mater. Sci. Lett. 1 (1982) 327–329.
[14] P.L. Swanson, C.J. Fairbanks, B.R. Lawn, Y.-W. Mai, B.J. Hockey, Crack-interface grain bridging as a fracture resistance mechanism in ceramics: I, experimental study on alumina, J. Am. Ceram. Soc. 70 (1987) 279–289.
[15] R.F. Cook, Segregation effects in the fracture of brittle materials: Ca-Al_2O_3, Acta Metall. Mater. 38 (1990) 1083–1100.
[16] M.V. Swain, R-curve behavior in a polycrystalline alumina material, J. Mater. Sci. Lett. 5 (1986) 1313–1315.
[17] K. Syassen, Ruby under pressure, High Pressure Res. 28 (2008) 75–126.
[18] R.A. Forman, G.J. Piermarini, J.D. Barnett, S. Block, Pressure measurement made by the utilization of ruby sharp-line luminescence, Science 176 (1972) 284–285.
[19] G.A. Myers, C.A. Michaels, R.F. Cook, Quantitative mapping of stress heterogeneity in polycrystalline alumina using hyperspectral fluorescence microscopy, Acta Mater. 106 (2016) 272–282.
[20] A.A. Kaplyanskii, A.K. Przhevuskii, R.B. Rozenbaum, Concentration-dependent lineshift in optical spectra of ruby, Sov. Phys. Solid State 10 (1969) 1864–1868.
[21] L. Grabner, Spectroscopic technique for the measurement of residual stress in sintered Al_2O_3, J. Appl. Phys. 49 (1978) 580–583.
[22] R.G. Munro, G.J. Piermarini, S. Block, W.B. Holzapfel, Model lineshape analysis for the ruby R lines used for pressure measurement, J. Appl. Phys. 57 (1985) 165–169.
[23] J. He, D.R. Clarke, Determination of the piezospectroscopic coefficients for chromium-doped sapphire, J. Am. Ceram. Soc. 78 (1995) 1347–1353.
[24] A.D. Chijioke, W.J. Nellis, A. Soldatov, I.F. Silvera, The ruby pressure standard to 150 GPa, J. Appl. Phys. 98 (2005) (114905-1-9).
[25] C.P. Ostertag, L.H. Robins, L.P. Cook, Cathodoluminescence measurement of strained alumina single crystals, J. Eur. Ceram. Soc. 7 (1991) 109–116.
[26] G.K. Banini, M.M. Chaudhri, T. Smith, I.P. Hayward, Measurement of residual stresses around Vickers indentations in a ruby crystal using a Raman luminescence microscope, J. Phys. D. Appl. Phys. 34 (2001) L122–L124.
[27] R. Sinclair, R.J. Young, R.D.S. Martin, Determination of the axial and radial fibre stress distributions for the Broutman test, Compos. Sci. Technol. 64 (2004) 181–189.
[28] Q. Ma, D.R. Clarke, Measurement of residual stresses in sapphire fiber composites using optical fluorescence, Acta Metall. Mater. 41 (1993) 1817–1823.
[29] Q. Ma, L.C. Liang, D.R. Clarke, J.W. Hutchinson, Mechanics of the push-out process from in situ measurement of the stress distribution along embedded sapphire fibers, Acta Metall. Mater. 42 (1994) 3299–3308.
[30] J.D. Belnap, D.K. Shetty, Interfacial properties of sapphire/epoxy composites: comparison of fluorescence spectroscopy and fiber push-in techniques, Compos. Sci. Technol. 65 (2005) 1851–1860.
[31] I. Fujishiro, Y. Nakamura, T. Kawazse, B. Okai, The property of a ruby high pressure sensor under uniaxial compressive stress, JSME Int. J. 31 (1988) 136–141.
[32] Q. Ma, D.R. Clarke, Piezospectroscopic determination of residual stresses in polycrystalline alumina, J. Am. Ceram. Soc. 77 (1994) 298–302.
[33] J. He, D.R. Clarke, Polarization dependence of the Cr^{3+} R-line fluorescence from sapphire and its application to crystal orientation and piezospectroscopic measurement, J. Am. Ceram. Soc. 80 (1997) 69–78.
[34] R.C. Powell, B. DiBartolo, Optical properties of heavily doped ruby, Phys. Status Solidi A 10 (1972) 315–357.
[35] B.R. Lawn, Fracture of Brittle Solids, 2 ed. Cambridge University Press, Cambridge, 1993.

[36] R.F. Cook, E.G. Liniger, R.W. Steinbrech, F. Deuerler, Sigmoidal indentation-strength characteristics of polycrystalline alumina, J. Am. Ceram. Soc. 77 (1994) 303–314.
[37] G.A. Myers, S.S. Hazra, M.P. de Boer, C.A. Michaels, S.J. Stranick, R.P. Koseski, R.F. Cook, F.W. DelRio, Stress mapping of micromachined polycrystalline silicon devices via confocal Raman microscopy, Appl. Phys. Lett. 104 (2014) (191908-1-5).
[38] G. Pezzotti, In situ study of fracture mechanisms in advanced ceramics using fluorescence and raman microprobe spectroscopy, J. Raman Spectrosc. 30 (1999) 867–875.
[39] J.A. Nychka, D.R. Clarke, Damage quantification in TBCs by photo-stimulated luminescence spectroscopy, Surf. Coat. Technol. 146-147 (2001) 110–116.
[40] A. Selçuk, A. Atkinson, The evolution of residual stress in thermally grown oxide on Pt diffusion bond coats in TBCs, Acta Mater. 51 (2003) 535–549.
[41] S. Guo, R.I. Todd, Cr^{3+} microspectroscopy measurements and modelling of local variations in surface grinding stresses in polycrystalline alumina, J. Eur. Ceram. Soc. 30 (2010) 2533–2545.
[42] O. Grasset, Calibration of the R ruby fluorescence lines in the pressure range [0–1 GPa] and the temperature range [250–300 K], High Pressure Res. 21 (2001) 139–157.
[43] G. Pezzotti, M.C. Munisso, K. Lessnau, W. Zhu, Quantitative assessments of residual stress fields at the surface of alumina hip joints, J. Biomed. Mater. Res. B Appl. Biomater. 95B (2010) 250–262.
[44] W. Zhu, G. Pezzotti, Tensor and spatially resolved analysis of microscopic stress fields in polycrystalline alumina by polarized Raman spectroscopy, Phys. Status Solidi A 208 (2011) 1141–1150.
[45] W. Zhu, G. Pezzotti, Raman analysis of three-dimensionally graded stress tensor components in sapphire, J. Appl. Phys. 109 (2011) (073502-1-13).
[46] N. Noguchi, A. Abduriyim, I. Shimizu, N. Kamegata, S. Odake, H. Kagi, Imaging of internal stress around a mineral inclusion in a sapphire crystal: application of micro-Raman and photoluminescence spectroscopy, J. Raman Spectrosc. 44 (2013) 147–154.
[47] M.C. Munisso, W. Zhu, G. Pezzotti, Raman tensor analysis of sapphire single crystal and its application to define crystallographic orientation in polycrystalline alumina, Phys. Status Solidi B 246 (2009) 1893–1900.
[48] W. Zhu, G. Pezzotti, Phonon deformation potentials for the corundum structure of sapphire, J. Raman Spectrosc. 42 (2011) 2015–2025.
[49] G. Pezzotti, W. Zhu, Resolving stress tensor components in space from polarized Raman spectra: polycrystalline alumina, Phys. Chem. Chem. Phys. 17 (2015) 2608–2627.
[50] P.K. Withers, H.K.D.H. Bhadeshia, Overview. Residual stress. Part I – measurement techniques, Mater. Sci. Technol. 17 (2001) 355–365.
[51] N.S. Rossini, M. Dassisti, K.Y. Benyounis, A.G. Olabi, Methods of measuring residual stresses in components, Mater. Des. 35 (2012) 572–588.
[52] M.D. Vaudin, Y.B. Gerbig, S.J. Stranick, R.F. Cook, Comparison of nanoscale measurements of strain and stress using electron back scattered diffraction and confocal Raman microscopy, Appl. Phys. Lett. 93 (2008) (193116-1-4).
[53] Y.B. Gerbig, S.J. Stranick, R.F. Cook, Measurement of residual stress field anisotropy at indentations in silicon, Scr. Mater. 63 (2010) 512–515.
[54] R.P. Koseski, W.A. Osborn, S.J. Stranick, F.W. DelRio, M.D. Vaudin, T. Dao, V.H. Adams, R.F. Cook, Micro-scale measurement and modeling of stress in silicon surrounding a tungsten-filled through-silicon via, J. Appl. Phys. 110 (2011) (073517-1-10).
[55] M.D. Vaudin, G. Stan, Y.B. Gerbig, R.F. Cook, High resolution surface morphology measurements using EBSD cross-correlation techniques and AFM, Ultramicroscopy 111 (2011) 1206–1213.
[56] J.A. Howell, M.D. Vaudin, R.F. Cook, Orientation, stress, and strain in an (001) barium titanate single crystal with 90° lamellar domains determined using electron backscatter diffraction, J. Mater. Sci. 49 (2014) 2213–2224.
[57] M.D. Vaudin, W.A. Osborn, L.H. Friedman, J.M. Gorham, R.F. Cook, Designing a standard for strain mapping: HR-EBSD analysis of SiGe thin film structures on Si, Ultramicroscopy 148 (2015) 94–104.
[58] L.H. Friedman, M.D. Vaudin, S.J. Stranick, G. Stan, Y.B. Gerbig, W.A. Osborn, R.F. Cook, Assessing strain mapping by electron backscatter diffraction and confocal Raman microscopy using wedge-indented Si, Ultramicroscopy 163 (2016) 75–86.